Roger Bostelman
National Institute of Standards and Technology,
Gaithersburg, MD 20899

Ji-Chul Ryu
Department of Mechanical Engineering,
University of Delaware,
Newark, DE 19716

Tommy Chang
National Institute of Standards and Technology,
Gaithersburg, MD 20899

Joshua Johnson
Florida Gulf Coast University,
Fort Myers, FL 33965

Sunil K. Agrawal
Department of Mechanical Engineering,
University of Delaware,
Newark, DE 19716
e-mail: agrawal@udel.edu

An Advanced Patient Lift and Transfer Device for the Home

The home lift, position, and rehabilitation (HLPR) chair has a unique design and novel capabilities when compared with conventional powered wheelchairs. In addition to mobility, it provides lift and can transfer patients. Even though medical devices are developing at a rapid pace today, an aspect that is often overlooked in these developments is adherence to "rider safety standards." The contributions of this paper are threefold: (i) novel design of a lift and transfer system, (ii) experiments and results toward improved stability test designs that include HLPR-type devices to meet rider safety standards, and (iii) autonomous navigation and control based on nonlinear system theory of dynamic feedback linearization. Stability experimental results show promise for multipurpose patient mobility, lift, and transfer devices such as HLPR. A method for autonomous maneuvers was tested in simulation and experiments. We also expect the autonomous or semi-autonomous mobility mode of the vehicle to be useful for riders who have potential neural and cognitive impairments. [DOI: 10.1115/1.4001255]

1 Introduction

Caregivers and nurses often have to lift patients and seat them into wheelchairs, beds, or automobiles. It is estimated that one out of every two nonambulatory patients falls and becomes injured when being transferred from a bed to a wheelchair [1]. In addition, one in every three nurses becomes injured from the physical exertion of moving nonambulatory patients [2]. According to current statistics, the number of people in the United States, 65 years or older, will double in the next 25 years. In 1950, there were 8 adults available to support each elder 65 or older. Today, the ratio is 5:1 and by 2020 this ratio will drop to 3 working age adults per elderly person [3]. A survey conducted by the NIST showed that there is a need for devices that provide mobility, lift, and can transfer patients so that subjects can reach upper shelves, or be placed on toilets, chairs, beds, and bathtubs [4]. The literature survey [4] showed that mobility devices today are not combined with patient transfer devices or rehabilitation devices. The combination of patient mobility with lift is minimally available today. Intelligent mobility is being researched where algorithms are applied to powered chairs to move a patient autonomously although without patient transfer. Individually, mobility devices, transfer devices, or rehabilitation devices are commercially available; some are operated by caregivers and some by patients.

Mobility devices include manual/powered chairs and scooters with power-assisted manual wheelchairs [5]. Intelligent mobility has been studied by several research organizations with examples provided in Refs. [6–8]. These intelligent devices have made excellent strides toward a robotic chair, e.g., to improve mobility of patients with severe and multiple disabilities through cluttered environments with graphical user interfaces. Researchers have provided a demonstration of docking a wheelchair with a separate patient sling lift [9]. All of these devices utilized off-the-shelf powered chairs without onboard patient lift, patient transfer, or rehabilitation capabilities.

Dependent care patient lift devices include manual/powered hydraulic rolling beds and chairs. These operate around the following user actions: Patient pivots out of the chair, patient stands, and patient's sling is attached to a Hoyer lift or a rolling lift mounted to a wall, bed, or ceiling. Independent care patient lifts include trapeze-style, ceiling-mounted cable lifts, stair lifts, wheelchair-to-vehicle lifts, and some automobile-mounted patient lift devices. All of these devices provide only a part of the lift required by the patient. Also, many of these lift devices require significant patient and/or even caregiver strength to move the patient to a chair, bed, or toilet.

The organization of this paper is as follows: The design of the HLPR chair is outlined in Sec. 2. Characterization of the safety standards for the chair is discussed in Sec. 3. These are followed by a novel trajectory planner and controller that uses the theory of dynamic feedback linearization in Sec. 4. Preliminary experiments that implement the autonomous controller with the HLPR chair are described in Sec. 5.

2 Design of HLPR Chair

HLPR chair, as shown in Fig. 1, is built around an off-the-shelf forklift. The forklift includes a U-frame base with two passive casters in the front and an actively steered and forward driven rear wheel. The lift and chair frame is 58 cm wide, 109 cm long, and 193 cm high, when not in the lifted position. It can pass through residential bathroom doors, as small as 61 cm wide and 203 cm high. The base and seat frames can be lifted 0.9 m from the seated position. The patient seat structure consists of two nested L-shaped frames. The outer L is a seat frame that provides lift and rotation point for the inner L seat frame. The L frames are made of square aluminum tubing welded as shown in the photograph. The outer L is bolted to the lift device while the inner L rotates with respect to the seat base frame at the end of the L, as shown in Fig. 1.

The rotation point for the frame is above the casters at the front of the HLPR chair frame. This feature allows for outside wheelbase access when the seat is rotated by 180 deg. Drive and steering motors, batteries, and control electronics, along with an aluminum support frame, provide counterweight for the patient to rotate beyond the wheelbase. When not rotated, the center of gravity remains near the middle of the HLPR chair. When rotated to 180 deg with a 136 kg subject on board, the center of gravity remains within the wheelbase for safe seat access.

Manuscript received October 7, 2009; final manuscript received January 22, 2010; published online March 26, 2010. Assoc. Editor: Ted Conway.

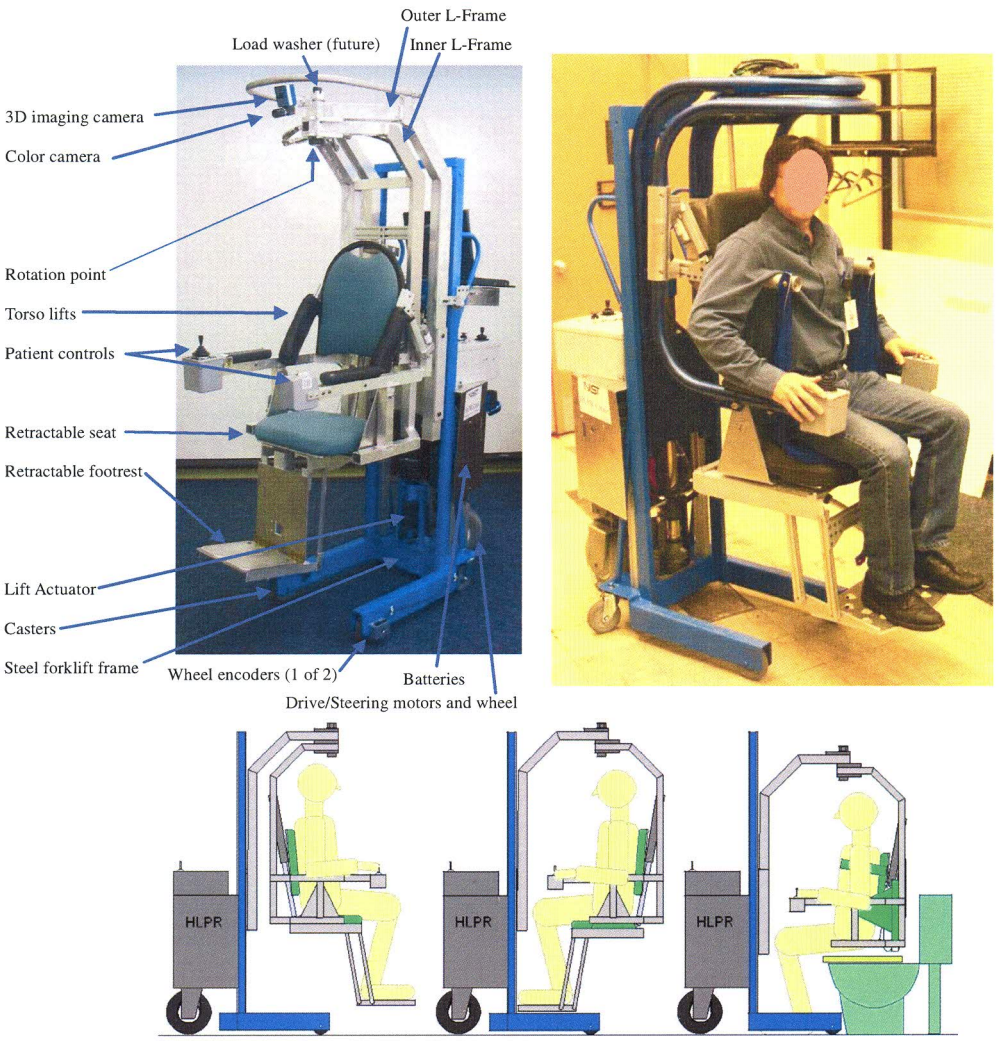

Fig. 1 HLPR chair prototypes 1 and 2. Graphics showing the concept of placing a patient onto a toilet or a chair.

Steering is reverse Ackerman controlled. The left joystick rotates the drive wheel counterclockwise and the right rotates the drive wheel clockwise. The drive motor is mounted perpendicular to the floor above the drive wheel with a chain drive. HLPR chair is powered similar to powered chairs using batteries. Two prototypes of HLPR chair have been built: The first was used to test stability and autonomous control and the second to study ergonomics and manufacturability of the seat and sling designs.

3 Stability Tests

Rider safety on the HLPR chair is characterized by safe loading, motion on sloped and tilted ramps, brake capability, and lift height. The stability tests were designed based on existing standards for wheelchairs and forklifts given by ANSI, RESNA, and ISO [10–13].

3.1 Static Stability Tests. A test platform measuring 2.4 $\times 1.2$ m^2 was designed, as shown in Fig. 2, to perform static stability tests on the HLPR chair. The platform, made out of extruded aluminum framing and plywood base, was lifted by a hoist on one end. Safety straps were attached to the HLPR chair during all tests. Slip prevention bars were also attached to the platform to prevent the HLPR chair from slipping down the ramp as the platform was tilted. A payload of 114 kg was used on the chair.

In these tests, the discrete tip angle was measured by placing a piece of paper under the tipping wheel, as suggested by the above standards. When the paper could easily be removed from beneath the wheel, the angle was recorded. The test was not designed to measure mechanical failures or device durability. Instead, the discrete tip angle in the most and least stable configuration was found. Factors that affect these results include load/lift height, load orientation, and HLPR orientation on the test platform. Load height was chosen to be a medium height of 1.3 m and a high height of 1.8 m. Figure 2 shows a series of example test configurations including the forward, side, and rear tilt configurations of the HLPR chair frame. The figure also shows a series of seat orientations including forward, side, and rear orientations with respect to the frame. The results of the static stability test are summarized in Fig. 2.

3.2 Dynamic Stability Tests. In dynamic stability tests, we studied loss of contact of the load-bearing wheels when the platform angle relative to horizontal was changed to 0 deg, 3 deg, 6 deg, and 9 deg, respectively. Dynamic tests included rearward dynamic stability on a ramp, forward dynamic stability on a ramp, lateral dynamic stability on a ramp, lateral dynamic stability while

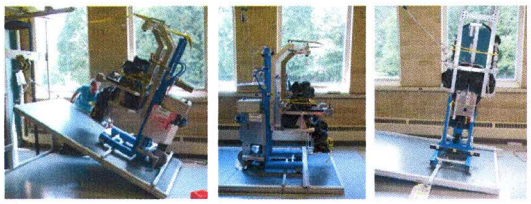

(a)

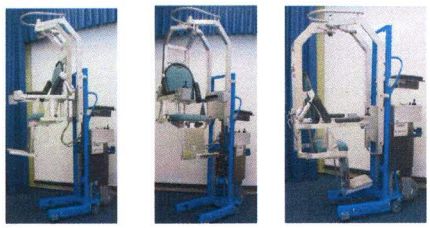

(b)

Test Configuration	Seat Orientation to Frame	Ramp Angle	
		Medium Load Height 1.3 m	High Load Height 1.8 m
Forward	Forward	18.4°	12.9°
	Side (90°)	17.8°	12.7°
	Rear	17.3°	12.2°
Lateral	Forward	8.0°	4.9°
	Side (90°)	8.1°	4.8°
	Rear	8.7°	5.1°
Rear	Forward	>25°	>25°
	Side (90°)	>25°	>25°
	Rear	>25°	>25°

(c)

Fig. 2 Static stability test configurations and results showing (*a*) (left to right) rear, forward, and lateral HLPR chair frames; (*b*) (left to right) forward, side, and rear seat orientations of the HLPR chair with respect to the frame; and (*c*) table of static stability test results

turning in circles, lateral dynamic stability while turning suddenly, and dynamic stability while traversing a step. The results were based on the severity of the lost wheel contact with the ground, drive, caster, or stabilizing wheel, as listed in Fig. 3. Figure 3 shows a passenger as the payload, approximately 93 kg, for forward tests.

A second platform was designed and built to support the HLPR chair dynamic stability measurements. This platform measured approximately 2.4 m wide × 3.7 m long and was built as a modular platform to disassemble into three approximately 1.2 × 2.4 m^2 sections while built to ANSI specifications to allow sufficient wheelchair travel. The platform was capable of tilting, using hand crank winches, to 0 deg, 3 deg, 6 deg, and 9 deg angles.

Sand bags were used as payloads for all rear and lateral tests. The snapshot shows a passenger ready to drive forward at full speed and turn left. Extreme caution was taken to prevent passenger harm by using straps and the presence of a second test operator. Dynamic stability test start positions were chosen to ensure that the HLPR chair would not traverse off the platform. Dynamic stability test results are summarized in Fig. 4.

4 Planner and Controller for HLPR Chair

Most wheelchairs are differentially driven through their wheels; i.e., if the right wheel is spun faster than the left wheel, the vehicle moves toward the left and if both wheels spin at the same rate, the vehicle travels straight. This is also the principle for manual drive of wheelchairs. However, due to its unique design, the HLPR chair is driven and steered through its rear wheel. This allows the motors and drive electronics to be placed behind the user and makes it compact and safe.

In this section, we describe a method for trajectory planning and control of the HLPR chair, which exploits its nonholonomic constraints, resulting from no-slip constraints of the wheels, to show that this system is dynamic feedback linearizable. With this property, the system is controllable and represented by a chain of integrators [14,15]. This form is then used to efficiently plan and control the motion of the vehicle. A schematic of the HLPR chair is shown in Fig. 5. The rear wheel of the HLPR chair is both driven and steered, whereas the front wheels are not steered. Hence, the inputs to this system are the driving speed u and the steering angle of the rear wheel ϕ.

In Cartesian coordinates, the system's configuration is given by

$$\mathbf{q} = [x, y, \theta, \phi]^T \tag{1}$$

where (x, y) is the position of the midpoint O between the two front wheels. θ is the orientation of the vehicle with respect to the X-axis and ϕ is the steering angle of the rear wheel with respect to the forward direction of the vehicle. L is the length from the midpoint O to the center of the rear wheel.

From the assumption of no-slip condition on the front and rear wheels, one can obtain the nonholonomic constraints of the form

$$\mathbf{C}(\mathbf{q})\dot{\mathbf{q}} = 0 \tag{2}$$

where

$$\mathbf{C}(\mathbf{q}) = \begin{pmatrix} \sin(\theta+\phi) & -\cos(\theta+\phi) & -L\cos\phi & 0 \\ \sin\theta & -\cos\theta & 0 & 0 \end{pmatrix} \tag{3}$$

With a matrix $\mathbf{S}(\mathbf{q})$ spanning the null space of $\mathbf{C}(\mathbf{q})$, it is possible to define a velocity vector $\boldsymbol{\nu}$ such that

$$\dot{\mathbf{q}} = \mathbf{S}(\mathbf{q})\boldsymbol{\nu} \tag{4}$$

where

$$\boldsymbol{\nu} = [u, \dot{\phi}]^T \tag{5}$$

$$\mathbf{S}(\mathbf{q}) = \begin{pmatrix} \cos\phi\cos\theta & 0 \\ \cos\phi\sin\theta & 0 \\ \sin\phi/L & 0 \\ 0 & 1 \end{pmatrix} \tag{6}$$

Here, u is the driving speed of the rear wheel at R_1. $\dot{\phi}$ represents the turning rate of the rear wheel. Therefore, Eq. (4) represents the kinematic model of the system. On defining

$$v = u\cos\phi \tag{7a}$$

$$w = \dot{\phi} \tag{7b}$$

the kinematic model of the system becomes

$$\begin{aligned} \dot{x} &= v\cos\theta \\ \dot{y} &= v\sin\theta \\ \dot{\theta} &= \frac{\tan\phi}{L}v \\ \dot{\phi} &= w \end{aligned} \tag{8}$$

By considering additional states z_1 and z_2 such that $z_1 = v$ and $z_2 = \dot{v}$, the prolonged system is given by

Test	Method of Retardation	Stability Score Ramp Angle (°)				Comments
		0	3	6	10	
Rearward Dynamic Stability						
Starting Forward		3	3	3	3	Slipping occurs at 3°
Stopping after traveling forward	R Release	3	3	3	3	Slipping occurs at 3°
	P Power off	3	3	3	3	Slipping occurs at 3°
	A Applying reverse	3	3	3	3	Slipping occurs at 3°
Braking when traveling backward	R Release	3	3	3	3	Slipping occurs at 3°
	P Power off	3	3	3	3	Slipping occurs at 3°
	A Applying reverse	3	3	3	3	Slipping occurs at 3°
Forward Dynamic Stability						
Braking when traveling forward	R Release	3	3	3	3	Slipping occurs at 3°
	P Power off	3	3	3	3	Slipping occurs at 3°
	A Applying reverse	3	3	3	3	Slipping occurs at 3°
Traveling forward down a slope onto a horizontal surface	N/A	N/A	3	3	0 2	Complete tip Transient tip
Dynamic Stability in Lateral Directions						
Turning on a slope	N/A	3	2	2	0	Transient tip on highest positioned front wheel
Turning suddenly at maximum speed	N/A	3	N/A	N/A	N/A	

(*a*)

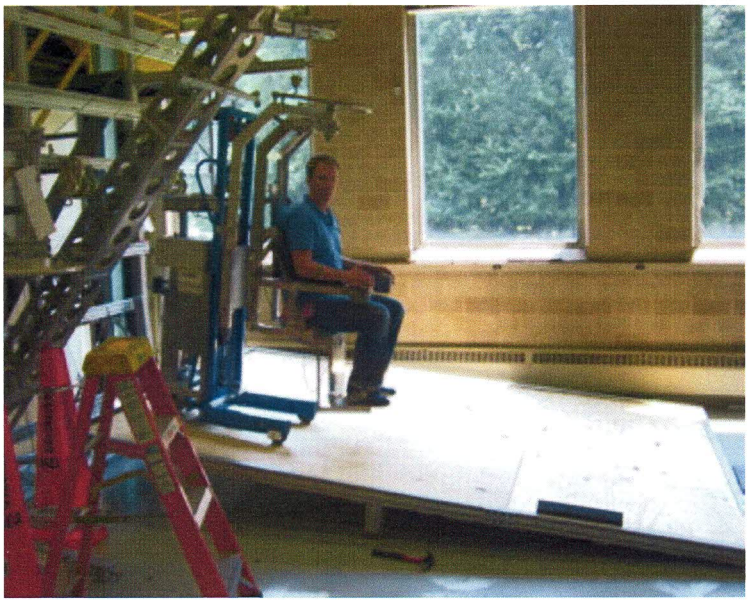

(*b*)

Fig. 3 (*a*) Dynamic stability test results. (*b*) The photo shows the start position of a starting forward test.

$$\dot{x} = z_1 \cos\theta$$
$$\dot{y} = z_1 \sin\theta$$
$$\dot{\theta} = \frac{\tan\phi}{L} z_1$$
$$\dot{\phi} = \bar{u}_2$$
$$\dot{z}_1 = z_2$$
$$\dot{z}_2 = \bar{u}_1 \tag{9}$$

where $\bar{u}_1$ and $\bar{u}_2$ are new inputs that satisfy

$$\bar{u}_1 = \ddot{v}, \quad \bar{u}_2 = w \tag{10}$$

Test	Stability Score		
	25 mm step height		
	1	2	3
Rearward Dynamic Stability			
Travelling forward up a step transition from a standing start	3	3	3
Travelling backward down a step transition from a standing start	3	3	3
Forward Dynamic Stability			
Travelling forward up a step transition at maximum speed	3	3	3
Traveling forward down a step transition from a standing start	3	3	3
Dynamic Stability in Lateral Direction			
One side of HLPR drops down a step transition	3	3	3

Fig. 4 Dynamic stability while traversing a step test results using a horizontal test surface instead of a 10 deg ramp as suggested by current standards with scores ranging from 0 (full tip) to 3 (no tip)

By choosing the outputs $\mathbf{F}=(F_1,F_2)=(x,y)$, all state variables and inputs in the prolonged system can be expressed in terms of these outputs and their derivatives from Eq. (9). These expressions are

$$(x,y)=(F_1,F_2) \tag{11}$$

$$z_1=\sqrt{\dot{F}_1^2+\dot{F}_2^2} \tag{12}$$

$$\theta=\tan^{-1}\left(\frac{\dot{F}_2}{\dot{F}_1}\right) \tag{13}$$

$$z_2=\dot{z}_1=\frac{\dot{F}_1\ddot{F}_1+\dot{F}_2\ddot{F}_2}{\sqrt{\dot{F}_1^2+\dot{F}_2^2}} \tag{14}$$

$$\phi=\tan^{-1}\left(\frac{L\dot{\theta}}{z_1}\right)=\tan^{-1}\left(L\frac{\dot{F}_1\ddot{F}_2-\ddot{F}_1\dot{F}_2}{\dot{F}_1^2+\dot{F}_2^2}\frac{1}{\sqrt{\dot{F}_1^2+\dot{F}_2^2}}\right) \tag{15}$$

The inputs $\bar{u}_1$ and $\bar{u}_2$ have the expressions

$$\bar{u}_1=\dot{z}_2=\xi_1\dddot{F}_1+\xi_2\dddot{F}_2+\xi_3 \tag{16a}$$

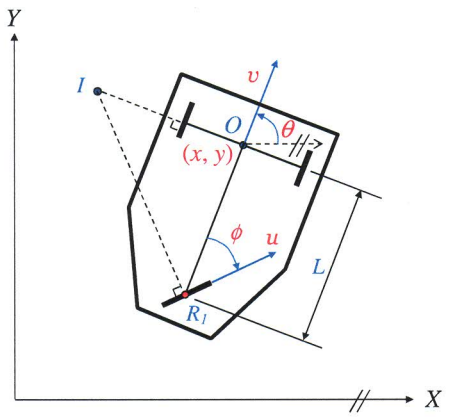

Fig. 5 The rear wheel-driven HLPR chair in Cartesian space described by (x, y, θ, ϕ). From the no-slip condition, the instantaneous center of rotation is located at *I*.

$$\bar{u}_2=\dot{\phi}=\zeta_1\dddot{F}_1+\zeta_2\dddot{F}_2+\zeta_3 \tag{16b}$$

where $\xi_i,\zeta_i(i=1,\ldots,3)$ are the functions of $\mathbf{F},\dot{\mathbf{F}},\ddot{\mathbf{F}}$. Hence, we are assured that F_1 and F_2 are properly chosen outputs and the HLPR chair described by the kinematic model in Eq. (9) is dynamically feedback linearizable. The diffeomorphism between the state variables and differentials of outputs is

$$F_1=x \tag{17a}$$

$$F_2=y \tag{17b}$$

$$\dot{F}_1=z_1\cos\theta \tag{17c}$$

$$\dot{F}_2=z_1\sin\theta \tag{17d}$$

$$\ddot{F}_1=z_2\cos\theta-z_1\dot{\theta}\sin\theta \tag{17e}$$

$$\ddot{F}_2=z_2\sin\theta+z_1\dot{\theta}\cos\theta \tag{17f}$$

where $\dot{\theta}$ was given in Eq. (9).

4.1 Trajectory Planning and Control. Over a given time period of $[t_0\ t_f]$, the end conditions given in the original system

$$x(t_0),y(t_0),\theta(t_0),\phi(t_0),z_1(t_0),z_2(t_0) \tag{18a}$$

$$x(t_f),y(t_f),\theta(t_f),\phi(t_f),z_1(t_f),z_2(t_f) \tag{18b}$$

can be transformed to

$$F_1(t_0),\dot{F}_1(t_0),\ddot{F}_1(t_0),F_2(t_0),\dot{F}_2(t_0),\ddot{F}_2(t_0) \tag{19a}$$

$$F_1(t_f),\dot{F}_1(t_f),\ddot{F}_1(t_f),F_2(t_f),\dot{F}_2(t_f),\ddot{F}_2(t_f) \tag{19b}$$

With choice of these trajectories as polynomials

$$F_{1d}(t)=a_5t^5+a_4t^4+a_3t^3+a_2t^2+a_1t+a_0 \tag{20}$$

$$F_{2d}(t)=b_5t^5+b_4t^4+b_3t^3+b_2t^2+b_1t+b_0 \tag{21}$$

the coefficients of these polynomials can be uniquely determined using the end conditions in Eq. (19).

From Eq. (16),

$$\begin{pmatrix}\dddot{F}_1\\ \dddot{F}_2\end{pmatrix}=\mathbf{A}+\mathbf{B}\begin{pmatrix}\bar{u}_1\\ \bar{u}_2\end{pmatrix} \tag{22}$$

where

$$\mathbf{A}=\begin{pmatrix}-z_1\dot{\theta}^2\cos\theta-3z_2\dot{\theta}\sin\theta\\ -z_1\dot{\theta}^2\sin\theta+3z_2\dot{\theta}\cos\theta\end{pmatrix},\quad \mathbf{B}=\begin{pmatrix}\cos\theta & -\dfrac{z_1^2\sin\theta}{L\cos^2\phi}\\ \sin\theta & \dfrac{z_1^2\cos\theta}{L\cos^2\phi}\end{pmatrix} \tag{23}$$

On redefining inputs, Eq. (22) can be written as

$$\dddot{F}_1=v_1 \tag{24a}$$

$$\dddot{F}_2=v_2 \tag{24b}$$

where

$$\begin{pmatrix}\bar{u}_1\\ \bar{u}_2\end{pmatrix}=\mathbf{B}^{-1}\left[\begin{pmatrix}v_1\\ v_2\end{pmatrix}-\mathbf{A}\right] \tag{25}$$

Feedback control laws for v_1 and v_2 can be proposed as

$$v_1=\ddot{F}_{1d}+k_2(\ddot{F}_{1d}-\ddot{F}_1)+k_1(\dot{F}_{1d}-\dot{F}_1)+k_0(F_{1d}-F_1) \tag{26a}$$

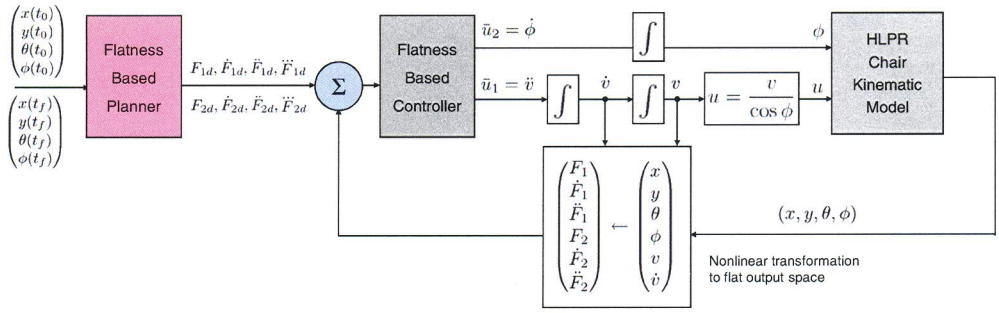

Fig. 6 The integrated planner and controller with the kinematic model of the HLPR chair

$$v_2 = \dddot{F}_{2d} + r_2(\ddot{F}_{2d} - \ddot{F}_2) + r_1(\dot{F}_{2d} - \dot{F}_2) + r_0(F_{2d} - F_2) \quad (26b)$$

where F_{1d} and F_{2d} are desired trajectories for the flat outputs F_1 and F_2, respectively, and k_i and r_i are control gains. Substituting these control laws given by Eq. (26) into Eq. (24) gives error dynamics of the closed-loop system expressed as

$$\ddot{e}_1 + k_2\ddot{e}_1 + k_1\dot{e}_1 + k_0 e_1 = 0 \quad (27)$$

$$\ddot{e}_2 + r_2\ddot{e}_2 + r_1\dot{e}_2 + r_0 e_2 = 0 \quad (28)$$

where $e_i = F_{id} - F_i$, $i = 1,2,3$. The control gains can be chosen such that all roots of the characteristic equations of the closed-loop error dynamics lie strictly in the left half-plane in order to ensure exponential stability.

By substituting Eq. (26) into Eq. (25), one can obtain the control inputs $\bar{u}_1$ and $\bar{u}_2$ for the prolonged system. Then, the original control inputs u and ϕ can be computed using Eqs. (7) and (10) and by integration.

4.2 Simulation Results. Fifth order polynomial desired trajectories over the time period of [0 10] s are generated for the flat outputs $F_1(t)$ and $F_2(t)$ with the following end conditions:

$$x(0) = 0, \quad y(0) = 0, \quad \theta(0) = \frac{\pi}{2}$$
$$\phi(0) = 0, \quad v(0) = 1, \quad \dot{v}(0) = 0 \quad (29)$$

$$x(10) = 10, \quad y(10) = 0, \quad \theta(10) = -\frac{\pi}{2}$$
$$\phi(10) = 0, \quad v(10) = 1, \quad \dot{v}(10) = 0 \quad (30)$$

Here, all units are in SI and angles are in radians. Consequently, the corresponding end conditions in the flat output space can be obtained through the diffeomorphism constructed in Eq. (17) as follows:

$$F_1(0) = 0, \quad \dot{F}_1(0) = 0, \quad \ddot{F}_1(0) = 0$$
$$F_2(0) = 0, \quad \dot{F}_2(0) = 1, \quad \ddot{F}_2(0) = 0 \quad (31)$$

$$F_1(10) = 10, \quad \dot{F}_1(10) = 0, \quad \ddot{F}_1(10) = 0$$
$$F_2(10) = 0, \quad \dot{F}_2(10) = -1, \quad \ddot{F}_2(10) = 0 \quad (32)$$

Using these end conditions, the coefficients of the fifth order polynomials given in Eqs. (20) and (21) can be uniquely determined. The desired trajectories of the vehicle's orientation θ and front wheel's angle ϕ are then automatically obtained from the designed trajectories of the flat outputs F_1 and F_2 using Eqs. (13) and (15), respectively. The control gains in Eq. (26) were selected so that all the roots of the characteristic equations of the error dynamics are at -2, and their values are $(k_0,k_1,k_2)=(8,12,6)$ and $(r_0,r_1,r_2)=(8,12,6)$. The structure of the integrated planner and controller, which is applied to the kinematic model of the HLPR chair, is shown in Fig. 6. Figure 7 shows the desired and actual trajectories of the HLPR chair. In this simulation, an initial error of 1.0 m in x at $t=0$ was given in order to show the exponential convergence to the desired trajectory. The desired and actual tra-

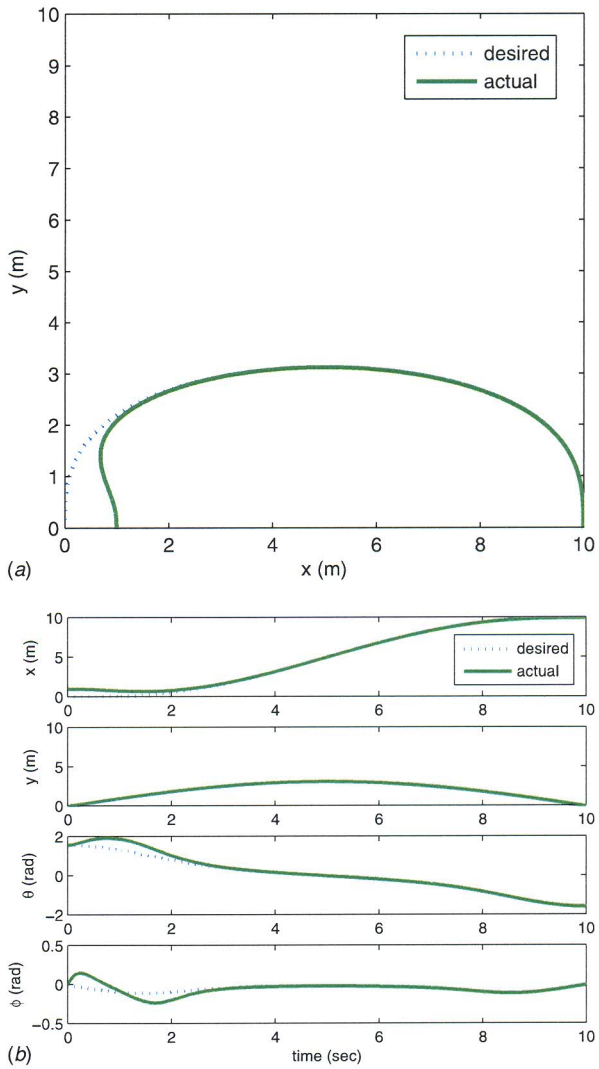

Fig. 7 (*a*) The desired and actual trajectories with the kinematic model-based controller. An initial error of 1 m in *x* is given to check the controller performance. (*b*) The state trajectories with the controller.

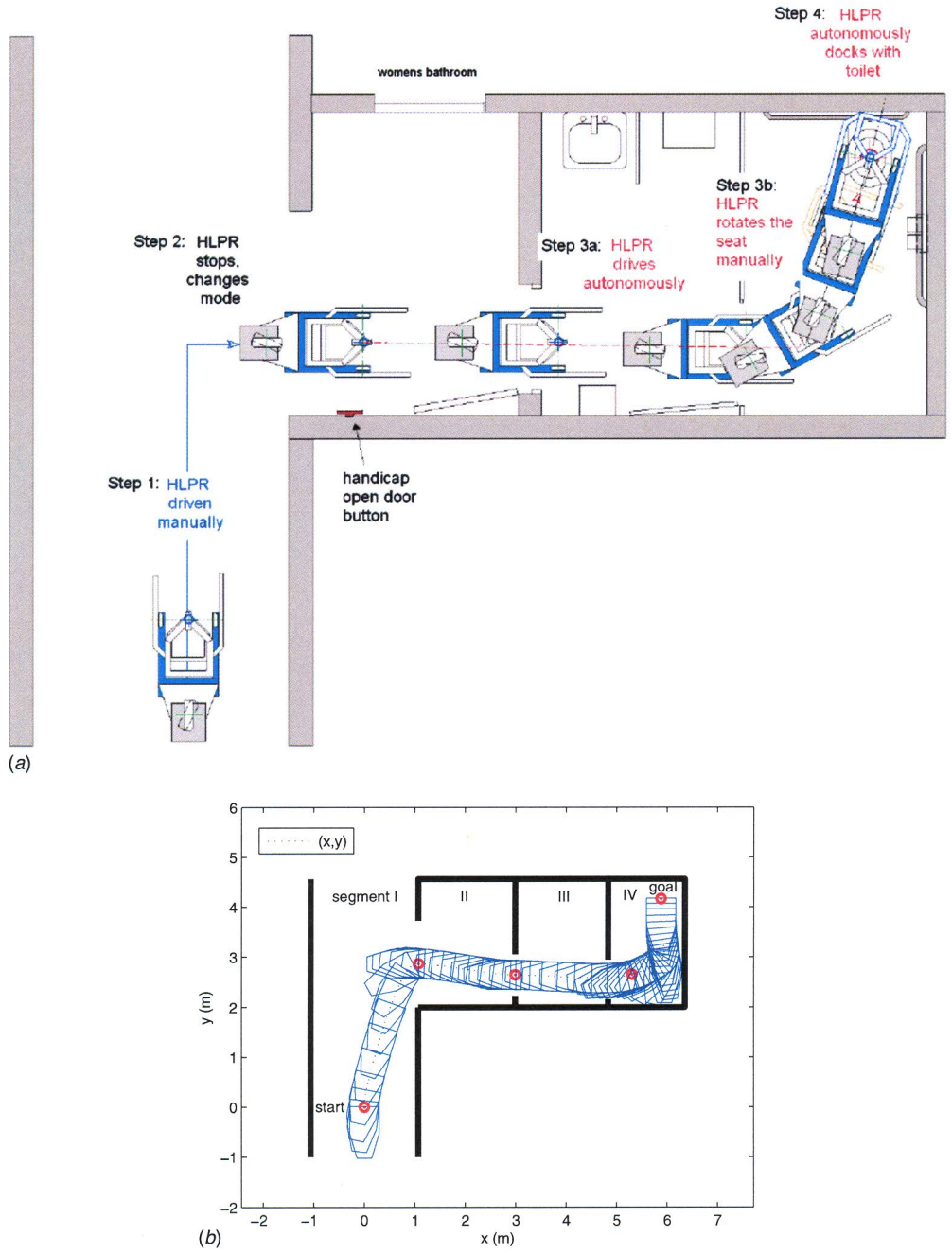

Fig. 8 (*a*) **A graphic top-view of a demonstration path to the toilet.** (*b*) **Computed path using the planner/controller.**

jectories of θ are shown in Fig. 7. The simulation results check the validity of the tracking controller for the kinematic model.

5 Simulation and Experiments of a Complete Maneuver

A complete autonomous maneuver of the HLPR chair is now discussed when it navigates through a narrow doorway and docks with the toilet. After docking, the HLPR chair will reverse its motion and navigate back to the starting position. A graphic view of this path is shown in Fig. 8. In Sec. 4, the desired trajectory was generated without considerations of obstacle avoidance. However, now the vehicle size should be taken into account. One way to solve this is to use higher order polynomials with additional coefficients, which are determined using optimization techniques.

Our approach was to divide the entire path into segments by choosing via points. Higher degree polynomials are used for each segment between two adjacent via points, while ensuring continuity at these points. The HLPR chair's shape was simplified to a polygon, as shown in Fig. 8. The six vertices of the polygon were used as constraint points to avoid collision with the walls. Figure 8 shows the simulation results, where snapshots were taken at every second. The state conditions used in the simulation are listed in Table 1. The travel time for each segment is 10 s except for the last segment, which is 20 s due to the limited space in the area.

Table 1 State variable conditions

Points	x (m)	y (m)	θ (rad)	ϕ (rad)	v (m/s)	$\dot{v}$ (m/s^2)
Start	0	0	$\pi/2$	0	0.1	0
Via point 1	1.067	2.864	0	0	0.1	0
Via point 2	2.985	2.642	0	0	0.1	0
Via point 3	5.297[a]	2.653	0.343[a]	0	0.1	0
Goal	5.875	4.165	$\pi/2$	0	0.1	0

[a]Determined by optimization.

Fig. 9 Sequential video captures of the HLPR chair following via points in a laboratory demonstration to enter and dock with a toilet

The HLPR chair was programed to follow via points just as shown in the simulation. Via points, doorways and wall corner locations were measured and laid out using tape spots and cones in a NIST laboratory. The HLPR chair ran through the maze of cones after being positioned above the first via point driving the entire way to the toilet without hitting any cones. Figure 9 shows snapshots of the autonomous HLPR chair demonstration to enter and dock with a toilet.

6 Conclusions

The HLPR chair has been prototyped in two versions. Static and dynamic stability tests were completed using the first HLPR chair prototype. Stability tests were designed based on ANSI, RESNA, and ISO standards. The results showed higher than expected tilt angles than required by the static stability test standards. During dynamic stability testing, the HLPR frequently slipped before tipping occurred. As to be expected based on static performance, the HLPR experienced transient tipping or complete tipping when undergoing dynamic lateral stability testing. Also, HLPR traveling forward up or down an incline set at 10 deg transitioning to/from step, as suggested by the standards, caused either transient or complete tipping, and tests were therefore halted by the researchers for safety concerns. HLPR chair is not designed to travel down steep ramps and transition steps from these ramps, but is meant to traverse doorway thresholds from horizontal surfaces. The tests shown in Fig. 4 were therefore performed with HLPR transitioned from a horizontal surface to/from a step. For these tests, results showed no tip issues as shown in the table. An integrated autonomous trajectory planner and controller was developed for this chair, which is driven by a novel rear wheel and steered with that wheel as well. This controller was based on dynamic feedback linearization of the governing nonlinear model. This integrated planner and controller was demonstrated to work well both in simulations and initial experiments with the prototype.

Acknowledgment

We appreciate the expertise offered by medical experts at conferences and Walter Reed Army Medical Center for their input to the HLPR chair usefulness and design modifications.

References

[1] U.S. Bureau of Labor Statistics, 1994, from Blevins website http://www.patientlift.net/282164.html.
[2] Blevins, H. S., 2006, Blevins Medical, Inc., http://www.patientlift.net/282164.html.
[3] Wasatch Digital iQ, 2003, InTouch health's remote presence robot used by healthcare experts, http://www.wasatchdigitaliq.com, Santa Barbara, CA and Salt Lake City, UT, Business Wire, Jun. 16.
[4] Bostelman, R., and Albus, J., 2006, "Survey of Patient Mobility and Lift Technologies Toward Advancements and Standards," NISTIR No. 7384.
[5] Bertocci, G., and Fitzgerald, S., 2006, "Rehabilitation Engineering Research Center on Wheelchair Transportation Safety," NIDRR/DOE, Oct.
[6] Kim, C., Kim, S., and Kim, B., 2000, "RTAI Based Real-Time Control of Robotic Wheelchair," Department of Electrical Engineering and Computer Science, Korea Advanced Institute of Science and Technology, Guseong-dong, Yuseong-gu, Daejeon, Korea.
[7] Communication Aids for Language and Learning Centre, 2001, Scotland, http://CALLCentre.education.ed.ac.uk/Smart_WheelCh/What_is_it_SWA/what_is_ it_swa.html#collision.
[8] Yanco, H. A., Hazel, A., Peacock, A., Smith, S., and Wintermute, H., 1995, "Initial Report on Wellesley: A Robotic Wheelchair System," Proceedings of the Workshop on Developing AI Applications for the Disabled, Internat. Joint Conf. on Artificial Intelligence, Montreal, Canada, August 1995.
[9] Song, W.-K., Lee, H., and Bien, Z., 1999, "KAIST—KARES: Intelligent Wheelchair-Mounted Robotic Arm System Using Vision and Force Sensor," Rob. Auton. Syst., **28**(1), pp. 83–94.
[10] ANSI/RESNA, Wheelchairs—Volume 1: Requirements and test methods for wheelchairs (including scooters).
[11] ISO 7176-1, Wheelchairs—Part 1: Determination of static stability.
[12] ISO 7176-2, Wheelchairs—Part 2: Determination of dynamic stability of electric wheelchairs.
[13] ISO 1074, Counterbalanced fork-lift trucks—Stability tests standard.
[14] Fliess, M., Levine, J., Martin, P., and Rouchon, P., 1995, "Flatness and Defect of Non-Linear Systems: Introductory Theory and Examples," Int. J. Control, **61**(6), pp. 1327–1361.
[15] Sira-Ramirez, H., and Agrawal, S. K., 2004, *Differentially Flat Systems*, Dekker, New York.